Energy & Environmental Science

Exploiting Heat Transfer to Achieve Efficient Photoelectrochemical CO_2 Reduction under Light Concentration

Journal:	*Energy & Environmental Science*
Manuscript ID	EE-ART-12-2021-003957.R1
Article Type:	Paper
Date Submitted by the Author:	23-Mar-2022
Complete List of Authors:	Kistler, Tobias; Lawrence Berkeley National Laboratory, Chemical Sciences Division and Joint Center for Artificial Photosynthesis; Technical University of Munich, Walter Schottky Institute and Physics Department Um, Min Young; Lawrence Berkeley National Laboratory, Chemical Sciences Division and Joint Center for Artificial Photosynthesis Cooper, Jason; Lawrence Berkeley National Laboratory, Chemical Sciences Division and Joint Center for Artificial Photosynthesis Sharp, Ian; Technical University of Munich, Walter Schottky Institute and Physics Department Agbo, Peter; Lawrence Berkeley National Laboratory, Chemical Sciences Division and Joint Center for Artificial Photosynthesis

SCHOLARONE™
Manuscripts

Exploiting Heat Transfer to Achieve Efficient Photoelectrochemical CO_2 Reduction under Light Concentration

Tobias A. Kistler[1,2,3], Min Young Um[1,2], Jason K. Cooper[1,2], Ian D. Sharp[3], Peter Agbo[1,2,*]

[1]Chemical Sciences Division, Lawrence Berkeley National Laboratory, Berkeley, California 94720, USA

[2]Joint Center for Artificial Photosynthesis, Lawrence Berkeley National Laboratory, Berkeley, California 94720, USA

[3]Walter Schottky Institute and Physics Department, Technische Universität München, 85748 Garching, Germany

[*]Corresponding Author: pagbo@lbl.gov

Abstract

Photoelectrochemical (PEC) conversion of carbon dioxide into valuable chemicals and fuels represents a promising path towards combating anthropogenic CO_2 emissions. However, the limited conversion efficiencies, operation lifetimes and CO_2 utilization efficiencies of PEC devices currently prohibit their application beyond the laboratory scale. Here, a wireless device converting CO_2 and water into carbon monoxide and hydrogen at a peak solar conversion efficiency exceeding 16% under an illumination intensity of 5 suns is demonstrated. A CO/H_2 product ratio between 10 - 20 is measured during a 17 h stability test. Fluctuations in device performance are rigorously analyzed via deconvolution of electrochemical and photoabsorber contributions. It is demonstrated that beneficial heat dissipation is enabled by wireless integration of the photoabsorber and electrocatalyst components, accounting for roughly 10% of the achieved conversion efficiency, an achievement unattainable with physically separated photoabsorber and electrolyzer components.

Introduction

While mean planetary temperatures continue to rise due to increasing anthropogenic carbon dioxide emissions, many countries still depend heavily on fossil fuels.[1,2] Converting exhaust CO_2 into fuels and other valuable chemicals provides a promising pathway to reduce the impacts of climate change and move away from fossil fuels. Electrochemical (EC) CO_2 reduction is one of several options for industrial-scale CO_2 conversion.[3,4] Ideally, such a process will be driven by renewable energy sources such as wind or sunlight.

Solar-driven CO_2 reduction may be facilitated by connecting a photovoltaic (PV) element to a dark electrolyzer. Yet, these designs generally do not exploit the potential heat exchange between the photoabsorber and electrolyte, which is expected to improve the overall efficiency in fully-integrated, photoelectrochemical (PEC) cells. Such heat exchange is especially important when concentrated sunlight is used to illuminate the photoabsorber.[5] Liquid electrolyte that flows through the electrolyzer cools the PV, significantly increasing its efficiency at elevated light concentrations. The heated electrolyte subsequently raises the temperature of catalytically active sites, improving the reaction kinetics. While conceptually promising, to date this beneficial heat exchange has rarely been demonstrated in PEC cells, due to system complexity and insufficient data collection and analysis.[5]

Until now, systems consisting of physically separated PV and electrolyzer components have outperformed wireless, PEC devices. Solar-to-fuel (STF) conversion efficiencies up to 20% have been demonstrated with the former at 1 sun illumination intensity,[6–13] while the latter have reached only 10%.[14–17] Integration of the photoabsorber into the strongly alkaline environment usually present in CO_2 electrolyzers introduces durability challenges, hindering the employment of beneficial device design strategies developed for dark CO_2 electrolysis. So far there have been very few reports of membrane-electrode assembly (MEA)-type, PEC devices for CO_2 reduction,[14,18] despite persuasive arguments that MEA devices can offer lower

operating voltages than corresponding flow cells, with potentially increased lifetimes.[19,20] Similarly, there have been very few demonstrations of solar-driven CO_2 electrolysis using concentrated sunlight, even though semiconductor photoabsorbers are generally more efficient under modest light concentration if sufficient cooling is provided and the series resistance is low enough.[21–26]

Here, we describe a fully-integrated, wireless, PEC device converting CO_2 to carbon monoxide at a peak solar-to-CO (STCO) efficiency of 15%, while producing hydrogen at a solar-to-H_2 (STH) efficiency of 1%, resulting in a combined STF efficiency of 16%. This marks a 60% improvement in STF efficiency relative to previous reports of fully-integrated, wireless, PEC devices for CO_2 conversion.[14–17] During a 17 h trial, the CO/H_2 product ratio ranges between 20:1 and 10:1 with no permanent degradation observed in device performance. Fluctuations in the combined STF efficiency between 6% and 16% are shown to be the result of bubble accumulation in the relatively thick anode layer. Stability tests revealed that the photoabsorber temperature plays an important role for the STF efficiency, especially when the operating point lies near the maximum power point (MPP) of the PV. Consequently, by analyzing the operating current and voltage, we demonstrate how PV cooling via liquid electrolyte enabled noteworthy device performance enhancements.

Results and Discussion

Device architecture

At the center of our device lies the PV-integrated membrane (PIM), consisting of a triple-junction PV surrounded by a Selemion membrane, as detailed in previous reports[14,27] (**Fig. 1**a and **Fig. 1**c). Similar to a MEA, the PIM is sandwiched by two carbon paper substrates coated with catalysts, leaving the PV unobstructed. On the cathode side, a gold catalyst is deposited on a micro-porous layer (MPL) containing polytetrafluoroethylene, which creates a

hydrophobic micro-environment on the gas diffusion electrode.[28] Humidified CO_2 flows through the serpentine channels in the acrylic front endplate and diffuses through the carbon paper towards the catalyst. On the catalyst surface, CO_2 and H_2O are converted to CO and H_2, depending on local reaction conditions,[14,28–31] while generating hydroxide ions that diffuse through the anion exchange membrane and react to form O_2 on the anodic catalyst surface. On the anode side, the Ni catalyst is directly sputtered on the carbon fibers (no MPL), creating a more hydrophilic environment than at the cathode. This allows the potassium hydroxide anolyte to wet the surface of the catalyst as it flows through channels machined in the anodic endplate.

The PV sits in the middle of the catalytic structure and can be directly illuminated through the acrylic endplate (cathode side), reducing path-dependent light attenuation compared to devices that include catalysts or electrolytes in the illumination path. However, since the catalyst is placed around the PV, the effective illumination area (with respect to the overall device footprint) is reduced unless a lens is used to concentrate the light that would otherwise fall on the carbon paper onto the PV (**Fig. 1**b). Furthermore, employment of a lens may significantly reduce the material costs, as the area of the high-efficiency photoabsorber can be reduced compared to the total illumination area. The light concentration factor using a Fresnel lens is adjusted by changing the distance between the lens and the PEC cell (**Fig. S1**, ESI).

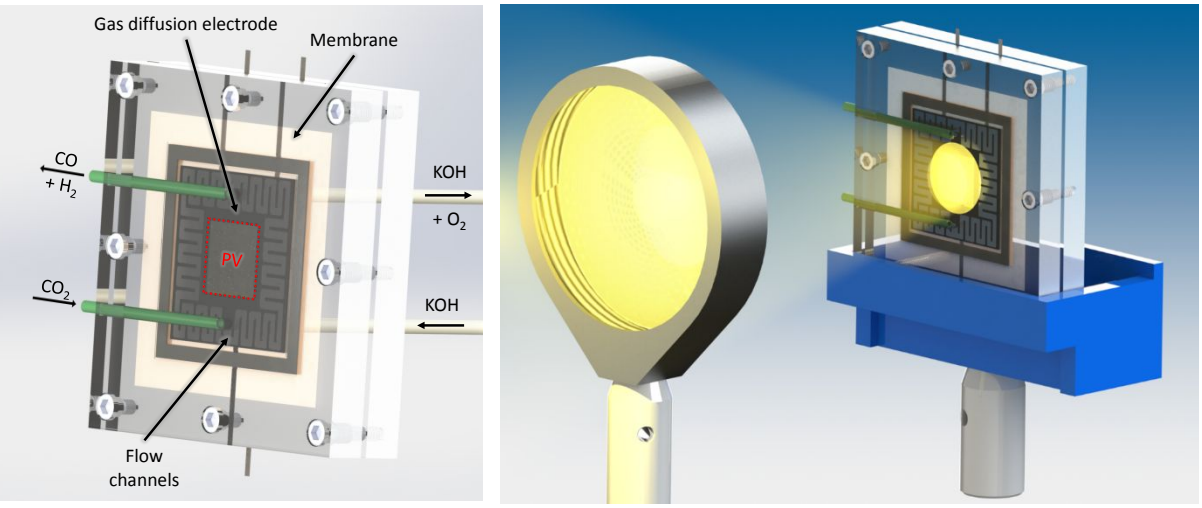

(a) (b)

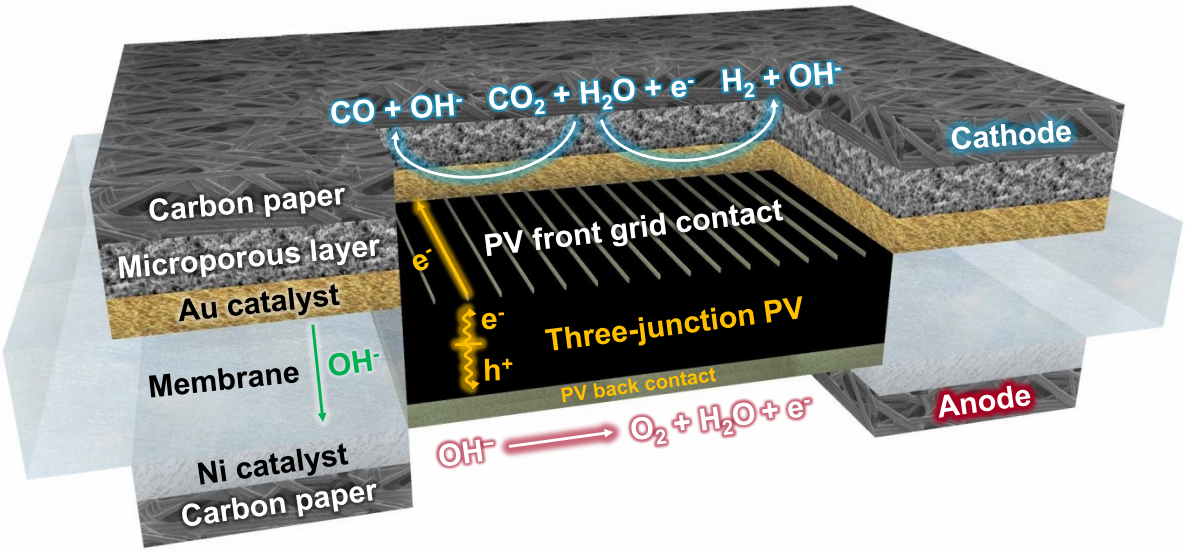

(c)

Fig. 1. Fully-integrated, wireless, PEC device used for light concentration testing. (a) PIM device performing PEC CO_2 reduction to CO and H_2. We note that the cathode outlet stream also contains unreacted CO_2 and the device design and operating conditions dictate the overall CO_2 utilization. (b) Fresnel lens concentrating the incoming light onto the PV of the PIM device. Moving the (green) cathodic inlet and outlet to the side of the cell enabled closer placement of the Fresnel lens to the PEC device. (c) Cross-section image showing the operating principle of the PIM device. The chemical reactions are shown without coefficients and the thickness of the layers are not to scale.

Electrochemical optimization for operation under light concentration

During PEC operation, the catalytic, EC components are coupled directly to the PV. Electroneutrality demands that the flux of electrical currents through series-linked components must be equal. As a result, the measured device current will be determined by the current-limiting component (PV or EC). To avoid significant efficiency penalties in a PEC device due to the shape of the PV polarization curve, the achievable EC current should equal or exceed the

PV short circuit current (I_{sc}) at a voltage slightly lower than at the MPP. Here, we define a critical voltage (V_{crit}), to prevent current drops in the PV polarization curve larger than 0.2% of I_{sc}. In other words, V_{crit} marks the point at which the PV polarization curve transitions from a flat line to an exponentially falling curve (see **Fig. S2**, ESI). In our case V_{crit} is ~2.1 V.

As mentioned above, illumination of the non-photoactive carbon paper should be avoided to maximize fuel production per total device area. Concentrating the light onto the photoabsorber increases its total output current provided to the catalytically active sites. Therefore, increasing the light concentration while keeping the catalyst area unchanged, requires optimizing the electrochemical activity of the catalyst to enable higher catalytic current densities at the same operating voltage.

The minimum concentration factor (c) to avoid losses of illumination area can be determined according to the respective areas of the catalyst (A_{cat}) and PV (A_{PV}):

$$c = \frac{A_{PV} + A_{cat}}{A_{PV}}. \#(1)$$

This results in the expected PV current under light concentration:

$$I_{PV} = j_{sc,\,1\,sun} \times c \times A_{PV}, \#(2)$$

with $j_{sc,\,1\,sun}$ describing the maximum achievable PV current density under short circuit conditions and 1 sun illumination intensity (no concentration).

Since the PV (equation 2) and EC ($I_{EC} = j_{EC} \times A_{cat}$) currents need to be equal, the EC current density (j_{EC}) can be calculated as a function of the PV and catalyst areas:

$$j_{EC} = j_{sc,\,1\,sun} \times \left(\frac{A_{PV}}{A_{cat}} + 1\right). \#(3)$$

Therefore, $j_{EC} \geq j_{sc,\,1\,sun}$ and using the parameters of the chosen PV (A_{PV} = 0.94 cm^2, $j_{sc,\,1\,sun}$ = 12.22 mA cm^{-2}) results in the blue current density as a function of the catalyst area curve shown in **Fig. 2**a.

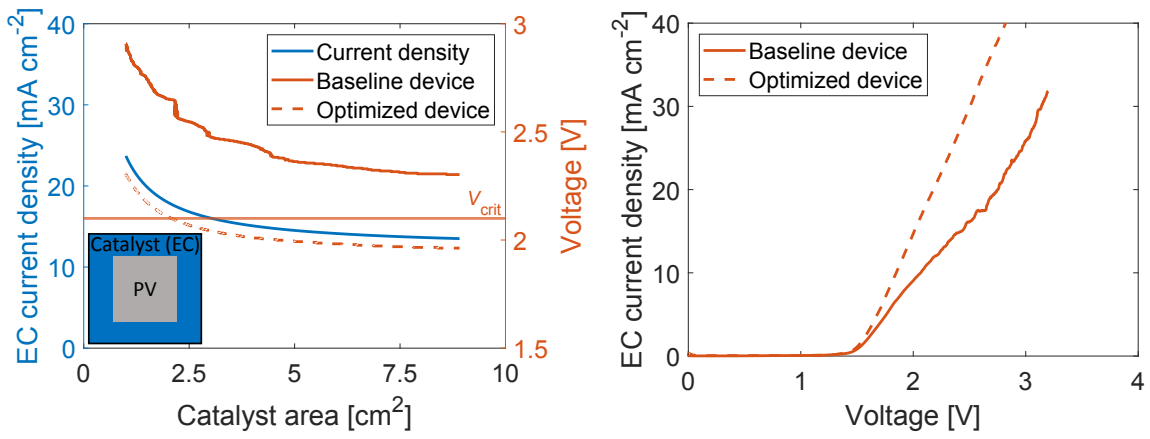

Fig. 2. Optimization of the EC performance. (a) Operating voltage and current density of the catalysts as a function of the geometric area. Optimization of the operating conditions for the baseline device was necessary to avoid current drops larger than 0.2% of I_{sc} by decreasing the operating voltage below V_{crit} (2.1 V). (b) EC CV curves of the baseline and optimized device, corresponding to the orange voltage curves in (a).

With a cyclic voltammogram (CV) measurement, the EC current density can be determined as a function of the applied voltage (**Fig. 2**b). With the data from the CV and the pre-determined current density curve from **Fig. 2**a, the expected operating voltage can then be determined as a function of the catalyst area (orange curves in **Fig. 2**a). Even though a larger catalyst area significantly reduces the operating voltage, using operating conditions similar to those described previously[14] (baseline device) will always lead to an operating point above V_{crit}. Since this would result in significant efficiency penalties, the operating conditions required optimizing catalyst activity to lower the operating voltage.

Similar to previous studies,[32–34] we found that Ir and Ni perform equally well as oxygen evolution reaction catalysts under the anodic conditions used in this study (**Fig. S3**, ESI). Hence, Ni catalysts supported on carbon paper were used for all subsequent experiments. The cathode's catalytic environment was tailored through the use of an MPL on the gas diffusion electrode, which resulted in favorable performance and shifted the product distribution towards CO

(**Fig. S4**, ESI). Moreover, the cathodic product ratio became independent of the cathodic inlet humidity when using the MPL (not shown here), in contrast to our previous findings without the MPL, which showed that higher humidity skewed the product distribution towards H_2.[14] The hydrophobic nature of the MPL prevents water molecules entering the cathode chamber from reaching the catalyst sites, resulting in high CO/H_2 product ratios throughout a broad range of cathodic humidities.

In addition, raising the concentration and flow rate of the KOH anolyte increased the current at an applied potential of 2 V (**Fig. S5 and S6**, ESI). Even though 5M KOH showed the highest currents, 2M KOH provided sufficient electrochemical performance at higher flow rates, while keeping the concentration of KOH at a minimum. However, it is important to note that higher KOH flow rates lead to increased CO_2 crossover through the membrane, accelerating acidification of the anolyte. Such acidification may result in a rapid current degradation, when a small anolyte reservoir is used (**Fig. S7**, ESI).

In summary, the addition of the MPL to the cathodic gas diffusion electrode, combined with a higher KOH anolyte concentration and flow rate, increased the current by a factor of 1.6-1.7 in the region of 2-2.1 V (optimized device in **Fig. 2**b). For a fixed PV area of 0.94 cm^2, this optimized performance now allows an expected operating voltage below V_{crit} for any catalyst area larger than 2.1 cm^2, with no significant voltage reductions occurring for areas beyond 5 cm^2. Given these considerations, we chose a catalyst area of 4 cm^2 to allow for small voltage fluctuations. The relative PV and EC areas thus require a light concentration factor of ~5 to minimize illumination of the non-photoactive EC element, while ensuring homogeneous illumination of the PV component in the integrated assembly.

Photoelectrochemical operation

Prior to PEC operation, the PV polarization response of a fully-assembled PIM device was evaluated using an external circuit at 1, 3 and 5 suns. The short circuit current density

scaled linearly with the light intensity (12.34, 36.23, and 62.07 mA cm^{-2}, respectively), the open circuit voltage increased from 2.65 V to 2.74 V, and only a minor reduction in fill factor (< 2% sun^{-1}) was observed (**Fig. S8**, ESI). The PV efficiency was between 27-28% for all three illumination intensities. We then added electrolyte (2M KOH, 5.9 mL min^{-1}) and humidified CO_2 (60 sccm) and conditioned the catalysts by biasing the system in the dark at 2 V for 50 min to achieve EC performance equilibration. This step allowed for the membrane to become equilibrated with anolyte and fully wet the cathode catalyst, which increased its electrochemically active surface area (**Fig. S9**, ESI).[14,35–37]

After equilibration, we established a direct connection between the PV and EC components to operate the PIM device in PEC mode, without external bias, at the three illumination intensities. At 1 sun, the current was stable at 12 mA during a 1 h trial, with a low operating voltage near 1.7 V due to the low EC current density needed at this light intensity (**Fig. S10**, ESI). As expected from the low operating voltage,[14] the product distribution heavily favored CO production, with a CO/H_2 product ratio near 30:1. By increasing the light intensity to 3.02 suns, the PEC current increased to 36 mA at 1.9 V (**Fig. S11**, ESI) and was again stable for a period of 1 h. The CO/H_2 product ratio was approximately the same at 30:1 as with 1-sun illumination.

At 5.05 suns, the optimized illumination intensity, the PIM device yielded a peak current near the short circuit current of the PV (**Fig. 3**a and **Fig. S12**a, ESI). The peak current was maintained for about 3 h before the current and voltage began to fluctuate. As the operating voltage rose above the voltage at the MPP (V_{MPP}), the current dropped significantly to about 50% of its peak value due to the large gradient of the PV polarization curve in this voltage region (**Fig. S12**a, ESI). Subsequent characterization strongly suggested that these increases in operating voltage are caused by O_2 bubble accumulation in the relatively thick carbon paper layer at the anode (see **Fig. S13**, ESI, Supporting Video and Experimental Section). Specifically, as the amount of trapped O_2 bubbles at the anode rises, more active sites for O_2 evolution are

blocked, effectively reducing the catalyst surface area and increasing the operating voltage (see **Fig. 2**a). When these trapped bubbles are suddenly released and swept away by the flowing electrolyte, the operating voltage quickly decreases and the current recovers to its peak value (**Fig. 3**a). Overall, there is no irreversible current degradation observed during the 17 h trial at 5.05 suns, with a peak current density normalized by the illumination intensity of 12.2 mA cm^{-2} sun^{-1} at an operating voltage of 2.05 V to 2.10 V. The excellent stability is further evidenced by the CVs of the PEC device before and after operation (**Fig. S12**b, ESI).

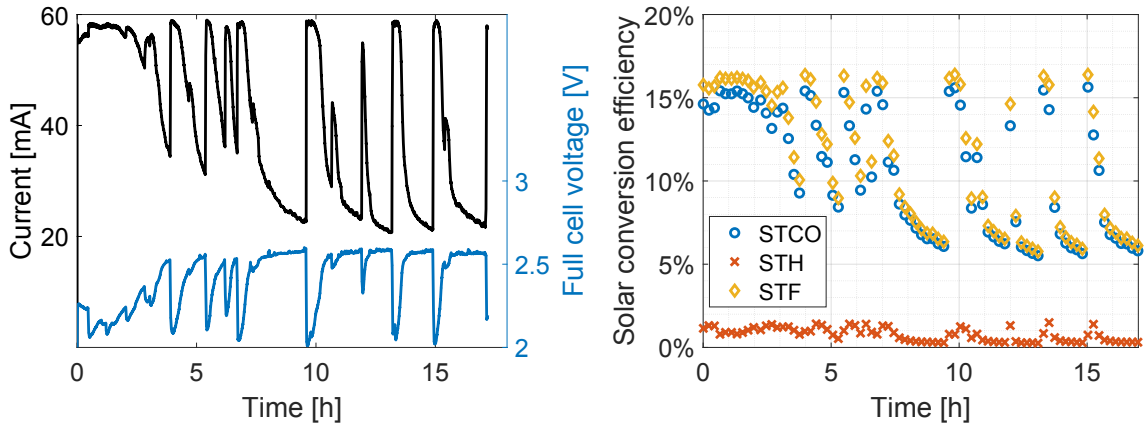

(a) (b)

Fig. 3. PEC device operation for 17 h at 5.05 suns illumination intensity without external bias. (a) Operating current and voltage. (b) STF energy conversion efficiencies.

The combined faradaic efficiency for CO and H_2 remained near 1 throughout the 17 h test, with a CO/H_2 product ratio ranging between 10:1 and 20:1 and an energy efficiency between 51-65% (**Fig. S12**c-e, ESI and Experimental Section). The slightly increased fraction of produced H_2 can be explained by the higher operating voltage compared to the 1- and 3-sun trials.[14] In particular, **Fig. S14** (ESI) shows the voltage dependence of the product ratio during this 17 h test. As the voltage increases, the product ratio moves towards increased H_2 generation until a turning point is reached near the V_{MPP} when the current starts to drop quickly. Therefore, for achieving both high currents and high CO/H_2 product ratios, it is important to maintain a low operating voltage.

With the amount of produced H_2 and CO, the respective solar conversion efficiencies can be calculated. The resulting STH efficiency is stable around 1% and the STCO efficiency ranges between 5.5-15.5% with a combined STF efficiency peak at 16.4% (**Fig. 3**b). The measured STF peak value marks a 60% relative increase compared to previous reports of fully-integrated, wireless, PEC devices.[14–17] In addition, it lies just below the theoretical maximum of 16.6%, as given by the PV short circuit current density measured directly after the 17 h trial and assuming a faradaic efficiency for CO of 100% (see Experimental Section and **Fig. S12**a, ESI).

Due to the high CO_2 flow rate used for this experiment, CO_2 utilization efficiencies were below 1%. However, CO_2 utilization efficiencies above 20% were achieved by reducing the CO_2 flow rate, with minimal reductions to the device current (~5%) (**Fig. S15**, ESI). Dilution of the CO_2 stream with N_2 at 10 sccm total flow rate also increased the CO_2 utilization by a factor of 5, with a 5% CO_2 feed showing the highest CO_2 utilization of 11% (**Fig. S16**, ESI).

Performance gains revealed through current-voltage analysis

As shown above in **Fig. 3**a, the operating current and voltage fluctuate considerably during the 17 h of PEC operation. Simultaneous collection of current and voltage data during steady-state operation (rather than merely logging device current over time) provides extra insight into device behavior and loss contributors.[38] In particular, the intersection of PV and EC performance curves indicates the expected operating point of the full PEC device at the beginning and end of operation (**Fig. 4**a and **Fig. S17**a, ESI). Similarly, concurrent measurement of voltage and current enables live tracking of the PEC operating point during unbiased operation. In this work, current logging is enabled by rerouting the electrons collected at the PV front surface through a potentiostat (shunt path)[27] before they hit the cathodic catalyst layer. The operating voltage can be measured between the PV front and back surface.

Any current deviation from the I_{sc} results in a performance decrease of the system. Similar to a previously disclosed method,[38] the encountered current losses may be deconvoluted into EC- and PV-related sources, provided that current and voltage are logged simultaneously, as described below. We note that, in contrast to our previously reported method, here the operating point is matched with a fitted EC curve instead of fitting a PV curve, which would require an assumption of unchanging, characteristic PV parameters such as shunt and series resistance during PEC device operation. PV fitting works well if it can be assumed that the PV temperature is constant and if its performance is mostly affected by partial shading, but EC fitting is preferred when the PV temperature over time is unknown.

As described above, bubble accumulation in the anode is likely the primary driving force for the elevated operating voltages. An increased amount of trapped bubbles will therefore reduce the usable area for catalysis, resulting in EC-related losses. Consequently, as a first deconvolution step, an EC curve is fitted through every measured operating point. For this fitting process, the EC curve shown in **Fig. 4**a is taken as a reference and then scaled by a factor that represents the percentage of usable EC surface area compared to the reference case, yielding EC curves intersecting with the extracted operating points. The resulting percentage of usable EC area was found to range from 25-125% (**Fig. S17**b, ESI). It should be noted that the reference case for the EC curve does not represent the highest possible polarization response for the electrocatalyst layer, allowing for the determination of relative, active areas over 100%.

After fitting the operating point to an appropriate EC curve, PV current losses may be determined by the difference of the measured current during operation and the corresponding current on the same EC curve but at the intersection with the initial PV curve (I_{init}, **Fig. 4**b). EC losses are then calculated by subtracting I_{init} from the current on the initial PV curve at 1.33 V, which is the minimum (thermodynamic) potential required for reducing CO_2 to CO.[39,40] While an increase in operating voltage naturally results in higher EC losses, it also makes the PEC

device performance more susceptible to changes in the PV fill factor due to temperature fluctuations.

During the 17 h of operation, the operating point fluctuates in the range bounded by the PV curves measured before and after operation (**Fig. 4**a). While it is difficult to determine the temperature of the PV in the PEC cell assembly, measurements of the PV temperature in the reference cell indicate a logarithmic increase over time as soon as the PV is illuminated, concurrent with a drop in PV fill factor (**Fig. S18**, ESI). Since both EC and PV losses are found to be essentially reversible, PV losses are most likely caused by PV heating, while EC losses are the result of catalyst overpotential increases due to bubble accumulation, as described above. As shown in **Fig. 4**c, the major loss process comes from the EC component, while the PV loss contribution makes up only roughly 5% of the total during most of the duration of the experiment (**Fig. S17**c, ESI).

Interestingly, when the operating points of the PEC device during the 17 h trial are compared to the PV curve measured after the trial, the majority lie above the final PV curve. The origin of this behavior is the reduction of the PV operating temperature by convective heat transfer to the liquid electrolyte flowing through the anolyte chamber. This increases the PV efficiency in accordance with the detailed balance model developed by Shockley and Queisser[41] (**Fig. S19**, ESI). The resulting current gains due to lower PV temperatures may be calculated by the difference of the operating current and the corresponding current on the same EC curve but at the intersection with the final PV curve (I_{final}, **Fig. 4**b). According to the current increases, up to 5% of the achieved STF efficiency was enabled by the lower PV temperatures during operation compared to the final PV temperature after the experiment (**Fig. S20**, ESI). However, to capture the full effect of electrolyte cooling, the operating point of the PIM device should be compared to a PV curve measured without active cooling under 5 suns illumination intensity (**Fig. S21**, ESI). This comparison highlights that more than 10% of the STF efficiency was enabled by cooling effects only available in a fully-integrated PEC device (**Fig. 4**d).

In summary, EC losses were the dominating factor for the observed current losses. Therefore, avoiding bubble accumulation in the anode chamber is the most effective way to stabilize device efficiencies. For instance, the flow channels and thickness of anodic carbon paper layer could be optimized to aid O_2 bubble transport. Furthermore, comparing the PEC operating point to a PV curve without active cooling highlights that more than 10% of the achieved solar conversion efficiency was enabled by cooling of the illuminated photoabsorber via electrolyte. While not described in detail here, the EC performance is also expected to benefit, in some measure, from the convective heat transfer between photoabsorber and catalyst surface facilitated by the electrolyte. Higher temperatures generally reduce the catalyst overpotential at a constant current due to the Arrhenius-type dependencies of reaction kinetics.[5] However, it is worth nothing that the electrolyte temperature increase due to illumination is rather small for the moderate concentration levels explored by this study (**Fig. S19**, ESI). Such temperature effects on reaction kinetics may become more relevant at higher levels of illumination.

Finally, it should be noted that efficiency gains from PV cooling are most significant at voltages near the MPP of the PV due to the shape of the PV polarization curve. Therefore, PV cooling will be most effective when the catalyst overpotentials are relatively high. However, industrially-relevant devices can be expected to be highly optimized and will likely operate close to the MPP of the PV to reduce costs and maximize efficiency (otherwise the photovoltage would be underutilized). Consequently, small fluctuations in catalyst overpotential will have a larger effect on overall efficiency without PV cooling due to reduced PV fill factors. As demonstrated in this report, beneficial heat transfer between electrolyzer and photoabsorber components can stabilize device performance while operating near the MPP, by keeping the PV fill factor high and reducing the catalyst overpotential.

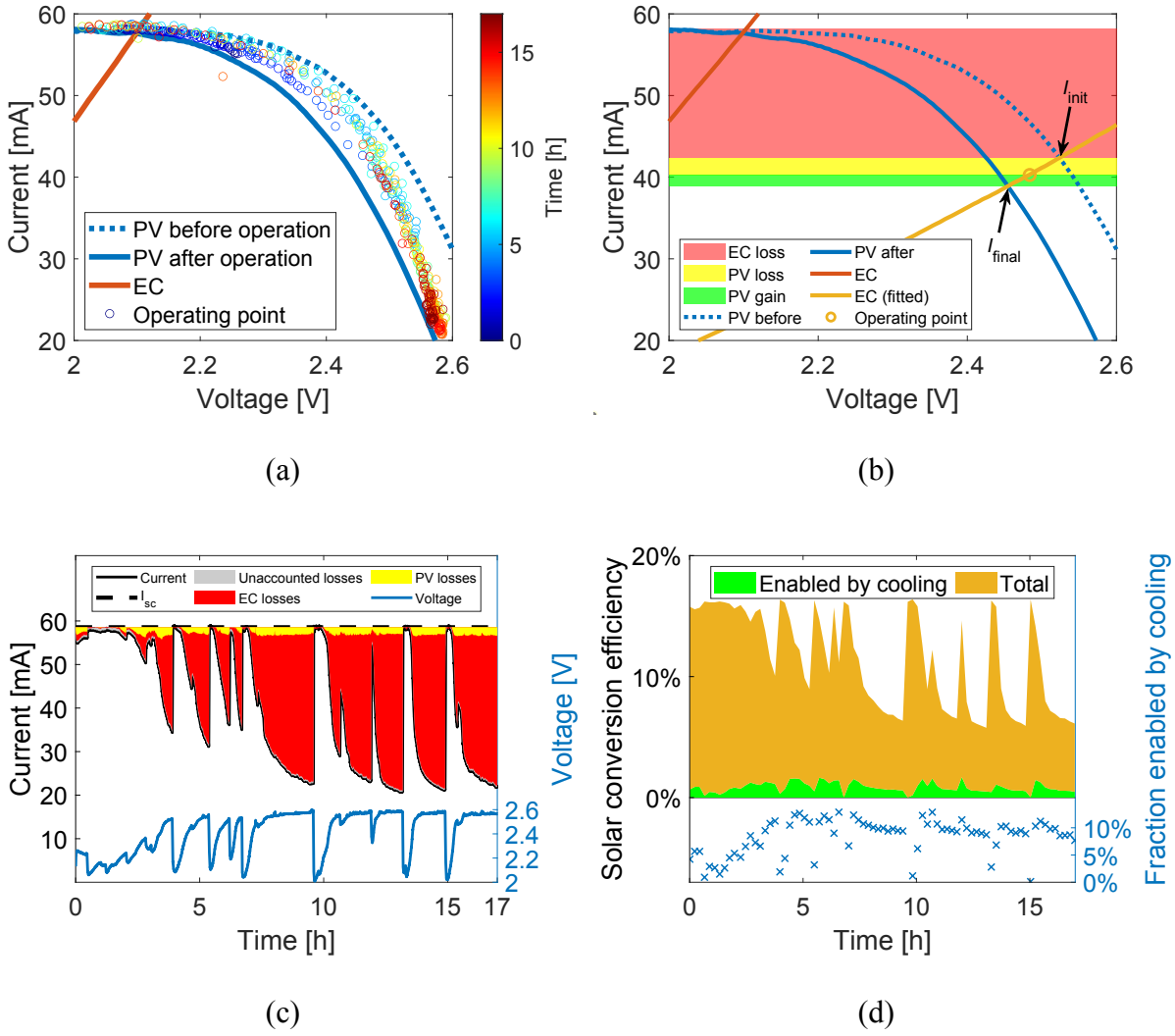

Fig. 4. Analysis of current fluctuations. (a) Comparison of the operating point during PEC operation to the PV and EC CV curves (see **Fig. S17**a, ESI for full-scale CVs). (b) Fitting of the EC curve to intersect with an operating point which subsequently allows specific determination of losses originating in the fully-integrated PV and EC elements. (c) Deconvoluted PV and EC losses during the 17 h trial. (d) Solar conversion efficiency of the PIM device enabled by cooling via electrolyte flow when compared to a PV without active cooling.

Surface analysis after operation

After the 17 h stability testing, we analyzed the surfaces of the catalyst-coated carbon papers using scanning electron microscopy (SEM) and energy dispersive X-ray spectroscopy

(EDS). The Ni-coated carbon paper did not show any signs of degradation but the Au-coated MPL delaminated from most of the carbon paper substrate upon device disassembly and adhered to the membrane (**Fig. S22**, ESI). However, as long as electrical contact between the catalyst and carbon paper substrate is maintained via mechanical compression, catalyst adhesion to the membrane is not expected to result in performance degradation. Indeed, the enhanced, interfacial contact between membrane and carbon paper substrate likely improves device performance. This accords with previous findings that anion-exchange membrane electrolyzers benefit from a catalyst coating directly on the membrane due to improved ionic transport.[42] Finally, the range of measured CO/H_2 product ratios did not change much during the 17 h trial (**Fig. S12**, ESI), further indicating a stable, catalytic environment.

Conclusion

We demonstrated 16% STF energy conversion efficiency in a fully-integrated, wireless, PEC device at an elevated illumination intensity of 5 suns. No permanent performance degradation could be detected during a 17 h stability test. Notably, analysis of the device polarization behavior over time revealed that, on average, 10% of the measured STF efficiency was enabled by convective PV cooling in this fully-integrated structure. Such benefits would have been inaccessible when using the same materials but physically separating the photoabsorber and electrochemically active components (PV-electrolyzer configuration). Finally, with this compact device structure, CO_2 utilization efficiencies can be increased from 1% to 20% by simply adjusting the CO_2 flow rate, an important step towards commercial viability.

Experimental Section

Deposition of catalysts

Untreated Toray TGP-H-60 carbon paper (Alfa Aesar) with a thickness of 200 μm served as substrate for the anodic Ni catalyst, while a 275 μm thick carbon paper coated with a MPL (AvCarb GDS2230) was used as substrate for the cathodic Au catalyst. The MPL contains polytetrafluoroethylene particles, introducing a strongly hydrophobic characteristic to the cathodic catalyst environment. The area of the carbon paper substrates was 4 cm^2 shaped similarly to a window frame, leaving a gap in the center to allow for illumination of the photoabsorber. All catalysts were deposited by radio frequency sputtering until a thickness of 100 nm was reached with catalyst loadings of 0.09 mg cm^{-2} for Ni and 0.19 mg cm^{-2} for Au.

Fabrication of the PIM and cell assembly

The fabrication of the PIM has been detailed previously.[14,27] Briefly, a square hole is cut into the membrane to make room for the PV. Then, a combination of epoxies is used to secure the PV in the membrane and to attach Ta metal strips which enable current-voltage analysis during operation. It should be noted that the PEC cell can operate without the Ta strips, which only serve analytical purposes. Since caustic KOH was used in the anode compartment, the PV back was covered with chemically-resistant epoxy. For this study, we used Selemion AMV membranes in the chloride form (~0.1 mm thick, AGC Engineering) and III-V triple-junction PVs from Spectrolab (XTE family). The PVs show a short circuit current density of ~14.07 mA cm^{-2}, open circuit voltage of ~2.69 V, fill factor of ~0.86 and efficiency of ~32.38% at 1 sun illumination intensity and before encapsulation. The PV front and back contacts consisted of 200 μm thick Au layers and the PV front was covered by an anti-reflective coating. Non-transparent epoxy covered the edges of the PV, likely reducing the illuminated area of the PV to slightly less than 0.94 cm^2. In fact, the short circuit current density dropped from ~14 mA cm^{-2} to 12.62 mA cm^{-2} after epoxy encapsulation. This drop in current density may be lowered by optimizing the amount of used epoxy or by deploying larger PVs where the area

near the edges represents a smaller fraction of the total area. Despite some expected area losses, an illuminated area of 0.94 cm^2 was considered for all efficiency calculations.

All cells were assembled by stacking the following layers from bottom to top: acrylic endplate with straight flow channels for the anolyte, carbon paper coated with the anodic catalyst and surrounded by a silicone gasket, PIM, Au-coated carbon paper surrounded by a silicone gasket, acrylic endplate with serpentine gas flow channels. For the PEC cell, three extra layers of uncoated carbon paper were placed in between the acrylic endplate and the Ni-coated carbon paper to make enough space for the epoxy-coated PV. Alternatively, a slot can be machined into the endplates. However, if the PV does not sit perfectly in that slot, nonuniform compression can easily damage the protective coating at the edges of the PV and promote pinhole formation. Therefore, we chose to create this slot with compressible carbon paper which allows for more flexibility during cell assembly. This also required a slightly higher torque (0.18 N m) when tightening the screws of the PEC cell compared to the EC cell (0.11 N m) to prevent leaks. However, the thick layer combined with the higher torque can hinder O_2 bubbles from leaving the anode catalyst surface and cause bubble accumulation.

Calibration of concentrated light intensity

A Newport Oriel Sol3A solar simulator equipped with a Xe lamp and AM1.5G filter was used for all illuminated experiments. To calibrate the light intensity under concentrated sunlight a Fresnel lens (2" diameter, Thorlabs FRP251) was first positioned at 1 sun illumination intensity using a monocrystalline silicon reference solar cell (Newport 91150V). The increased light intensity behind the Fresnel lens was then measured with a home-made reference cell, which mimics the composition, size and position of the photoabsorber in the PEC cell. The calibration of the home-made reference cell yielded a short circuit current density (j_{sc}) of 12.62 mA cm^{-2} at 1 sun and 25 °C with a temperature dependence of 0.009 mA cm^{-2} $°C^{-1}$. The measured j_{sc} as a function of the distance between the reference cell and Fresnel lens can then be correlated to

the light concentration factor, assuming direct proportion and correcting for the temperature (T) as the reference cell heats up:

$$c = \frac{j_{sc} - 0.009\ \text{mA cm}^{-2}\ ^{\circ}\text{C}^{-1} \times (T - 25\ ^{\circ}\text{C})}{12.62\ \text{mA cm}^{-2}}. \#(4)$$

Measurement conditions

If not otherwise mentioned, the following experimental conditions were used. A peristaltic pump pushed 2M KOH at a flow rate of ~6 mL min^{-1} through the anode chamber of the PEC cell. KOH electrolytes were prepared using ACS reagent grade pellets from Sigma-Aldrich. For all light-driven experiments, a KOH reservoir volume of ~200 mL was chosen to prevent acidification of the anolyte via CO_2 crossover during long-term experiments. CO_2 was first flowed at 60 sccm through a bubble humidifier filled with Milli-Q water (resistivity > 18.2 MΩ cm) kept at room temperature (~25 °C) and then into the cathode chamber. CVs were measured in a two-electrode configuration at scan rates of 10 mV s^{-1} for EC and PEC tests and 200 mV s^{-1} for PV tests. Dark EC stability measurements were carried out at a constant full cell potential of 2 V, while illuminated PEC tests were not biased by a potentiostat (0 V).

Product analysis

The cathode outlet was fed directly into a gas chromatograph from SRI Instruments (Multiple Gas Analyzer #5, 8610C) equipped with a thermal conductivity detector and flame ionization detector (FID). Prior to the FID, all products went through a methanizer to increase the minimum detection limit of the carbon-based products. The highest CO concentration available for calibration of the FID was 7980 ppm. If CO_2 utilization efficiencies surpass 1%, the CO concentration in the product stream will likely exceed the calibration limits. Therefore, the cathode outlet needs to be diluted with an inert gas such as argon to stay within the limits and

the linear range of the detector. To determine CO_2 utilization efficiencies, the CO molar flow in the cathode outlet stream was divided by the inlet CO_2 molar flow.

Microscopic characterization

The surface morphology and elemental composition was analyzed by SEM and EDS in an FEI Quanta 250 FEG system. An optical microscope (Olympus BX51) was used to analyze the non-conductive surface of the PIM.

Conversion efficiencies

With the minimum water splitting potential of 1.23 V at 25 °C, the STH efficiency can be calculated by dividing the produced H_2 through the illumination power density at 1 sun (0.1 W cm^{-2}), the size of the PV (0.94 cm^2) and the concentration factor:[6]

$$\mathrm{STH} = \frac{1.23\ \mathrm{V} \times I_{\mathrm{PV}} \times \text{faradaic efficiency}\ (\mathrm{H_2})}{0.1\ \mathrm{W\ cm^{-2}} \times A_{PV} \times c}. \#(5)$$

Similarly, the STCO efficiency is determined using the minimum cell potential of 1.33 V required for the cathodic evolution of CO:

$$\mathrm{STCO} = \frac{1.33\ \mathrm{V} \times I_{\mathrm{PV}} \times \text{faradaic efficiency}\ (\mathrm{CO})}{0.1\ \mathrm{W\ cm^{-2}} \times A_{PV} \times c}. \#(6)$$

Since no other products were observed (cumulative faradaic efficiency of measured products is near 1), the combined STF efficiency is the sum of the STH and STCO efficiencies.

Further, the energy/energetic efficiency (EE) towards H_2 and CO products is calculated via dividing the amount of energy used to form the aforementioned products by the net electrical energy supplied to the system:[2]

$$\mathrm{EE}_{\mathrm{H_2}} = \frac{1.23\ \mathrm{V}\ \times\ \text{faradaic efficiency}\ (\mathrm{H_2})}{\text{full cell voltage}}, \#(7)$$

$$\mathrm{EE}_{\mathrm{CO}} = \frac{1.33\ \mathrm{V}\ \times\ \text{faradaic efficiency}\ (\mathrm{CO})}{\text{full cell voltage}}. \#(8)$$

Acknowledgements

The authors thank David Larson for his helpful insights and Yalili Kistler for her help with the cross-section image. This study was conducted at the Joint Center for Artificial Photosynthesis (JCAP), a DOE Energy Innovation Hub, supported through the Office of Science of the U.S. Department of Energy under Award Number DE-SC0004993. TAK acknowledges support by the German Academic Exchange Service (DAAD, No. 57504612). IDS acknowledges support by the Federal Ministry of Education and Research (BMBF, Germany) project number 033RC021B within the CO_2-WIN initiative.

Conflict of Interest

The authors declare no competing interests.

References

1 R. U. Ayres and E. H. Ayres, *Crossing the Energy Divide. Moving from Fossil Fuel Dependence to a Clean-Energy Future*, Prentice Hall, Upper Saddle River, NJ, 2010.
2 R. Küngas, *J. Electrochem. Soc.*, 2020, **167**, 44508.
3 J. Zhang, W. Cai, F. X. Hu, H. Yang and B. Liu, *Chem. Sci.*, 2021, **12**, 6800–6819.
4 S. Garg, M. Li, A. Z. Weber, L. Ge, L. Li, V. Rudolph, G. Wang and T. E. Rufford, *J. Mater. Chem. A*, 2020, **8**, 1511–1544.
5 S. Tembhurne, F. Nandjou and S. Haussener, *Nat. Energy*, 2019, **4**, 399–407.
6 W.-H. Cheng, M. H. Richter, I. Sullivan, D. M. Larson, C. Xiang, B. S. Brunschwig and H. A. Atwater, *ACS Energy Lett.*, 2020, **5**, 470–476.

7 M. Asadi, M. H. Motevaselian, A. Moradzadeh, L. Majidi, M. Esmaeilirad, T. V. Sun, C. Liu, R. Bose, P. Abbasi, P. Zapol, A. P. Khodadoust, L. A. Curtiss, N. R. Aluru and A. Salehi-Khojin, *Adv. Energy Mater.*, 2019, **9**, 1803536.

8 M. Schreier, F. Héroguel, L. Steier, S. Ahmad, J. S. Luterbacher, M. T. Mayer, J. Luo and M. Grätzel, *Nat. Energy*, 2017, **2**, 17087.

9 M. Schreier, L. Curvat, F. Giordano, L. Steier, A. Abate, S. M. Zakeeruddin, J. Luo, M. T. Mayer and M. Grätzel, *Nat. Commun.*, 2015, **6**, 7326.

10 G. Gurudayal, J. Bullock, D. F. Srankó, C. M. Towle, Y. Lum, M. Hettick, M. C. Scott, A. Javey and J. Ager, *Energy Environ. Sci.*, 2017, **10**, 2222–2230.

11 F. Urbain, P. Tang, N. M. Carretero, T. Andreu, L. G. Gerling, C. Voz, J. Arbiol and J. R. Morante, *Energy Environ. Sci.*, 2017, **10**, 2256–2266.

12 Y. Xiao, Y. Qian, A. Chen, T. Qin, F. Zhang, H. Tang, Z. Qiu and B.-L. Lin, *J. Mater. Chem. A*, 2020, **8**, 18310–18317.

13 B. Kim, H. Seong, J. T. Song, K. Kwak, H. Song, Y. C. Tan, G. Park, D. Lee and J. Oh, *ACS Energy Lett.*, 2020, **5**, 749–757.

14 T. A. Kistler, M. Y. Um, J. K. Cooper, I. D. Sharp and P. Agbo, *Adv. Energy Mater.*, 2021, **11**, 2100070.

15 V. Andrei, B. Reuillard and E. Reisner, *Nat. Mater.*, 2020, **19**, 189–194.

16 T. Arai, S. Sato and T. Morikawa, *Energy Environ. Sci.*, 2015, **8**, 1998–2002.

17 M. Asadi, K. Kim, C. Liu, A. V. Addepalli, P. Abbasi, P. Yasaei, P. Phillips, A. Behranginia, J. M. Cerrato, R. Haasch, P. Zapol, B. Kumar, R. F. Klie, J. Abiade, L. A. Curtiss and A. Salehi-Khojin, *Science*, 2016, **353**, 467–470.

18 C. E. Creissen and M. Fontecave, *Adv. Energy Mater.*, 2020, **11**, 2002652.

19 L.-C. Weng, A. T. Bell and A. Z. Weber, *Energy Environ. Sci.*, 2019, **12**, 1950–1968.

20 C. M. Gabardo, C. P. O'Brien, J. P. Edwards, C. McCallum, Y. Xu, C.-T. Dinh, J. Li, E. H. Sargent and D. Sinton, *Joule*, 2019, **3**, 2777–2791.

21 J. F. Geisz, R. M. France, K. L. Schulte, M. A. Steiner, A. G. Norman, H. L. Guthrey, M. R. Young, T. Song and T. Moriarty, *Nat. Energy*, 2020, **32**, 326–335.

22 A. Royne, C. J. Dey and D. R. Mills, *Sol. Energy Mater. Sol. Cells*, 2005, **86**, 451–483.

23 A. Aldossary, S. Mahmoud and R. AL-Dadah, *Appl. Therm. Eng.*, 2016, **100**, 490–500.

24 G. Siefer and A. W. Bett, *Prog. Photovolt: Res. Appl.*, 2014, **22**, 515–524.

25 P. Singh and N. M. Ravindra, *Sol. Energy Mater. Sol. Cells*, 2012, **101**, 36–45.

26 A. Luque, *Solar cells and optics for photovoltaic concentration*, Adam Hilger, Bristol, 1989.

27 T. A. Kistler, N. Danilovic and P. Agbo, *J. Electrochem. Soc.*, 2019, **166**, H656.

28 L.-C. Weng, A. T. Bell and A. Z. Weber, *Phys. Chem. Chem. Phys.*, 2018, **20**, 16973–16984.

29 J. S. DuChene, G. Tagliabue, A. J. Welch, X. Li, W.-H. Cheng and H. A. Atwater, *Nano Lett.*, 2020, **20**, 2348–2358.

30 D. M. Koshy, S. Chen, D. U. Lee, M. B. Stevens, A. M. Abdellah, S. M. Dull, G. Chen, D. Nordlund, A. Gallo, C. Hahn, D. C. Higgins, Z. Bao and T. F. Jaramillo, *Angew. Chem.*, 2020, **132**, 4072–4079.

31 A. Goyal, G. Marcandalli, V. A. Mints and M. T. M. Koper, *J. Am. Chem. Soc.*, 2020, **142**, 4154–4161.

32 M. Tahir, L. Pan, F. Idrees, X. Zhang, L. Wang, J.-J. Zou and Z. L. Wang, *Nano Energy*, 2017, **37**, 136–157.

33 N.-T. Suen, S.-F. Hung, Q. Quan, N. Zhang, Y.-J. Xu and H. M. Chen, *Chem. Soc. Rev.*, 2017, **46**, 337–365.

34 C. C. L. McCrory, S. Jung, I. M. Ferrer, S. M. Chatman, J. C. Peters and T. F. Jaramillo, *J. Am. Chem. Soc.*, 2015, **137**, 4347–4357.

35 P. Connor, J. Schuch, B. Kaiser and W. Jaegermann, *Z. Phys. Chem.*, 2020, **234**, 979–994.

36 S. Trasatti and O. A. Petrii, *Pure Appl. Chem.*, 1991, **63**, 711–734.
37 M. C. O. Monteiro, F. Dattila, B. Hagedoorn, R. García-Muelas, N. López and M. T. M. Koper, *Nat. Catal.*, 2021.
38 T. A. Kistler and P. Agbo, *APL Mater.*, 2020, **8**, 31107.
39 S. Nitopi, E. Bertheussen, S. B. Scott, X. Liu, A. K. Engstfeld, S. Horch, B. Seger, I. E. L. Stephens, K. Chan, C. Hahn, J. K. Nørskov, T. F. Jaramillo and I. Chorkendorff, *Chem. Rev.*, 2019, **119**, 7610–7672.
40 K. P. Kuhl, E. R. Cave, D. N. Abram and T. F. Jaramillo, *Energy Environ. Sci.*, 2012, **5**, 7050.
41 W. Shockley and H. J. Queisser, *J. Appl. Phys.*, 1961, **32**, 510–519.
42 G. Lindquist, S. Oener, Q. Xu, A. R. Motz, A. Keane, C. Capuano, K. E. Ayers and S. W. Boettcher, *Meet. Abstr.*, 2020, **MA2020-02**, 2446.

Broader Context

Current trends in global mean temperatures indicate that mere reductions in carbon dioxide emissions will not be enough to combat global warming. Instead, it will eventually become necessary to deploy carbon-negative and carbon-neutral technologies such as electrochemical CO_2 reduction driven by renewable energy sources like solar. Respective devices generally consist of two main components: the first one converts solar energy into electrical energy which is then converted into chemical energy (such as fuels) by the second. The second component is usually made more efficient by employing catalysts. However, these catalytic materials generally deactivate over time, resulting in performance drops of electrochemical and photoelectrochemical (PEC) devices. In this report, we highlight how the performance of fully-integrated, PEC devices can be stabilized via thermal management relative to devices consisting of physically-separated solar conversion and fuel production components. We demonstrate this using a cell that employs beneficial design elements and materials developed for dark electrochemistry, resulting in the highest efficiency for fully-integrated PEC CO_2 reduction devices reported to date.